Check for updates

Journal of Chemistry

WILEY

RESEARCH ARTICLE OPEN ACCESS

Photocatalytic Reduction of Nitroaromatic Compounds Using NiO-Modified MgAl Hydrotalcite: A Sustainable Approach for Wastewater Treatment

Leimmy Calderon[1] | Daniela Barrera[1] | Claudia Castañeda[1] | Jose J. Martínez[1] | Hugo Rojas[1] | Francisco Tzompanzi[2] | Dora Solis[3] | Sonia Mancipe Estevez[1]

[1]Escuela de Ciencias Químicas Universidad Pedagógica y Tecnológica de Colombia UPTC, Avenida Central Del Norte, Vía Paipa, Tunja, Boyacá, Colombia | [2]Depto. De Química, Universidad Autónoma Metropolitana-Iztapalapa, D.F. México, Mexico | [3]Laboratorio de Nanotecnología, Universidad Autónoma Del Estado de México, Toluca de Lerdo, Mexico

Correspondence: Sonia Mancipe Estevez (sonia.mancipe@uptc.edu.co)

Received: 1 July 2025 | **Revised:** 11 December 2025 | **Accepted:** 31 December 2025

Academic Editor: Munmun Bardhan

Keywords: NiO/MgAl | nitrophenols | photocatalysis | reduction

ABSTRACT

The growing industrialization has caused the generation of highly toxic compounds such as nitroaromatic compounds. An adequate treatment to reduce the contamination of these organic compounds is necessary. The photocatalytic reduction of aromatic compounds using semiconductor materials favors the production of nitroaromatics. In the present work, NiO materials supported on MgAl hydrotalcite and with different NiO content (1 wt.%, 3 wt.%, 5 wt.%, and 10 wt.%) were synthesized by the co-precipitation method. The materials were characterized and evaluated in the photocatalytic reduction of 2,4-dinitrophenol (2,4-DNP) and 2,4,6-trinitrophenol (2,4,6-TNP). The characterization results revealed the formation of lamellar solids with features typical of layered double hydroxides. The photocatalytic evaluation showed that the NiO/MgAl 1 wt.% photocatalyst is efficient in the reduction of 2,4-DNP and 2,4,6-TNP. Furthermore, it was demonstrated that the reduction of 2,4-DNP is higher than 2,4,6-TNP. Additionally, it was verified that the photocatalytic reduction reaction proceeds via the photogenerated electrons, confirming the key role of the material in driving the reduction process.

1 | Introduction

Increasing industrialization has favored economic and social development; however, it has also increased pollution rates and the discharge of hazardous organic waste into the environment. It is widely acknowledged that many environmental pollutants are unavoidable outcomes of human activities, particularly industrialization, agricultural practices, and the improper disposal of wastewater represent a significant source of contamination [1]. The effects that pollutants present in industrial effluents have on the bodies of water, soil, and human health are diverse and heterogeneous. Adequate treatment of these polluted waters in hydraulic sources reduces the harmful effects and increases water reuse in different activities.

Nitroaromatic compounds and their derivatives are stable and soluble substances that cause a serious problem in wastewater from industry [2]. The nitroaromatic compounds are aromatic compounds in which the hydroxyl and nitro groups are directly attached to the aromatic ring. These substances are characterized by being carcinogenic and mutagenic, presenting a high risk to the life of mammals, and can seriously affect the aquatic system since they are widely used in the industry for the manufacture and processing of a variety of products such as pharmaceuticals,

This is an open access article under the terms of the Creative Commons Attribution License, which permits use, distribution and reproduction in any medium, provided the original work is properly cited.

Copyright © 2026 Leimmy Calderon et al. *Journal of Chemistry* published by John Wiley & Sons Ltd.

colorants, pigments, plastics, pesticides, fungicides, explosives, and industrial solvents [3]. The reduction of nitroaromatics to amines is of great importance in the pharmaceutical industry due to that the amines are reactive intermediates in the synthesis of paracetamol, acetanilide, and phenacetin [4, 5].

The development of different technologies for wastewater treatment includes traditional physical, biological, and chemical procedures, such as filtration [6, 7], microbial degradation [8, 9], electrocoagulation [10, 11], adsorption [12, 13], and electrochemical treatment [14, 15]; however, these have not been efficient enough for the treatment of nitroaromatic compounds. Advanced oxidation processes (AOPs) are an environmentally friendly, efficient, and economical technology and have been developed as an alternative in the treatment of polluting compounds from effluents, such as the electro-Fenton [16, 17], Fenton [18, 19], ozonation [20], photo-Fenton [21], degradation [22, 23], among others.

Heterogeneous photocatalysis is one of the most promising AOPs to carry out the oxidation–reduction reactions of polluting organic matter; it has been widely investigated due to its applications in chemical synthesis, energy innovation, and the removal of organic pollutants. Photocatalysis, driven by semiconductors such as NiO, offers a promising approach by harnessing the photocatalytic generation of reactive oxygen species (ROS) to treat organic pollutants and transform them into environmentally benign byproducts [24]. During the photocatalytic process, the absorption of light (visible or ultraviolet) by a semiconductor material takes place when absorbing the light favors that an electron of the valence band (VB) is excited towards the conduction band (CB), giving rise to the formation of the well-known electron–hole pair (e^-/h^+). The charge carriers migrate to the surface of the semiconductor so that oxidation or reduction reactions can take place there [25]. During the photocatalytic process for the reduction of nitrophenols using semiconductor materials, it is necessary to use sacrificial agents that allow greater efficiency in the activity. Among the most used agents are hydrazine (N_2H_4) [26], sodium sulfide (Na_2S) [27], methanol (CH_3OH) [28], sodium borohydride ($NaBH_4$) [29], sodium citrate ($C_6H_5Na_3O_7$) [30], and sodium sulfite (Na_2SO_3) [5]. The latter is a photostable compound that does not lead to the formation of toxic intermediates when used in oxidation–reduction reactions and promotes a basic medium.

In addition, it is interesting to know that during the photoreduction treatment of nitrophenols, it is possible to obtain amino derivatives, which are less toxic and essential compounds for the pharmaceutical industry [31]. Nickel (II) oxide (NiO) is a promising material for wastewater pollutant reduction. As a p-type semiconductor, it has a band gap energy ranging from 3.1 to 3.5 eV. On the other hand, the support of hydrotalcite-type materials allows that when a semiconductor such as NiO is dispersed, characteristics are obtained that improve the photoactivity of the catalytic material [32].

The layered double hydroxides (LDH), anionic clays or hydrotalcite-type materials, are a family of laminar compounds with anions in the interlaminar region. The structure of these compounds consists of $Mg(OH)_2$ brucite-type lamina, in which the partial substitution of the divalent cations by trivalent cations results in a positive residual charge that is compensated by anions that will be present in the interlaminar space. The formula for this type of material is $(M^{2+}_{1-x}M^{3+}_x(OH)_2)^{x+}(X^{n-}_{x/n}.mH_2O)$ where $x = 0.2 \leq x \leq 0.33$ and $M^{2+}$and M^{3+} are divalent and trivalent metal cations, respectively, which occupy the octahedral positions in the lamina and X^{n-} is the anion found within the interlaminar region along with some water molecules [33]. The present study shows the benefit of using NiO materials supported on hydrotalcite MgAl in photocatalytic reduction reactions of nitroaromatic compounds using Na_2SO_3, as a sacrificial agent, and UV radiation, as an alternative in the treatment of recalcitrant organic compounds. Several studies have reported the photocatalytic reduction of nitrophenols using different materials and conditions, as summarized in Table 1.

In this work, the photocatalytic reduction of the 2,4-dinitrophenol (2,4-DNP) and 2,4,6-trinitrophenol (2,4,6-TNP) contaminants under UV irradiation was evaluated. For this purpose, NiO materials supported on hydrotalcite MgAl were used as photocatalysts employing Na_2SO_3 as a sacrificial agent. This strategy will offer a more efficient and environmentally friendly alternative for treating recalcitrant organic pollutants compared to traditional methods.

NiO/MgAl materials significantly enhance photocatalytic activity. On the one hand, the homogeneous dispersion of NiO nanoparticles on the hydrotalcite surface prevents their agglomeration, thereby increasing the number of accessible active sites and optimizing light absorption efficiency. On the other hand, the structural and textural properties of hydrotalcite such as its large surface area, basicity, and the presence of interlayer anions facilitate a more efficient separation of electron–hole pairs and promote charge transfer processes during the photocatalytic reaction. This synergistic interaction between NiO and the MgAl support plays a crucial role in the reduction of nitroaromatic pollutants, while simultaneously improving the catalyst's stability and reusability.

Furthermore, the modification of MgAl hydrotalcite with NiO represents a more sustainable approach to wastewater treatment. This material not only enhances the reduction efficiency of recalcitrant organic compounds but also reduces the risk of secondary pollution due to its structural robustness and chemical stability under reaction conditions. In addition, the use of Na_2SO_3 as a sacrificial agent is more environmentally friendly compared to other commonly employed reductants, reinforcing the green character of the process. Altogether, NiO-supported MgAl hydrotalcite emerges as a highly promising photocatalyst, capable of combining efficiency, selectivity, and environmental compatibility, while offering a viable alternative for cleaner water resources and the recovery of amine intermediates of industrial relevance.

2 | Materials and Methods

2.1 | Synthesis of MgAl and NiO/MgAl

The synthesis of hydrotalcite MgAl was carried out by the coprecipitation method, mixing 0.23 mol of Mg $(NO_3)_2$•$6H_2O$ (Panreac 98%) and 0.075 mol Al $(NO_3)_3$•$9H_2O$ (Sigma-Aldrich 98%) maintaining a molar ratio of 3 together with 1.01 mol of CH_4N_2O (Panreac 98.5%), at a temperature of 60°C for 13 h and 400 rpm until homogenization. Subsequently, the hydrolysis of urea was carried out at 100°C for 10 h; the pH of the suspension

2962, 2026, 1, Downloaded from https://onlinelibrary.wiley.com/doi/10.1155/joch/1225741 by Sonia Mancipe Estevez - Cochrane Colombia , Wiley Online Library on [29/01/2026]. See the Terms and Conditions (https://onlinelibrary.wiley.com/terms-and-conditions) on Wiley Online Library for rules of use; OA articles are governed by the applicable Creative Commons License

TABLE 1 | Reported work on the photocatalytic reduction of nitrophenols.

Author/year	Photocatalyst	Target compound	Main observation	Reference
Nguyen et al./2019	Graphitic C_3N_4 with 2 wt.% Au	2,4-Dinitrophenol	High activity; recyclable ≥ 10 cycles; Cl^- enhances, $H_2PO_4^-$/SO_4^{2-}/HCO_3^-/NO_3^- inhibit; Au–H species detected; electron transfer is rate-limiting	[34]
Gerelbaatar et al./2018	AuNPs and AgNPs as catalyst	2,4-Dinitrophenol	AuNPs ($k = 1.24 \times 10^{-2}\ s^{-1}$) and AgNPs ($k = 8 \times 10^{-3}\ s^{-1}$) show high activity and stability for 2,4-DNP reduction with $NaBH_4$ under mild conditions	[35]
Ramu et al./2021	CuO/NiO nanoparticles	Nitrophenol, 2,4-dinitrophenol and 2,4,6-trinitrophenol	CuO/NiO NPs (25 nm, high crystallinity) reduced NP, DNP, and TNP within 2, 5, and 25 min, with $k = 1.519$, 0.5102, and 0.4601 min^{-1}, respectively; stable catalyst producing aminophenols	[36]
Phyu et al./2023	Bi_2MoO_6/carbon nitride heterojunction	Nitrophenol, 2,4-dinitrophenol, and 2,4,6-trinitrophenol	Bi_2MoO_6/PCN heterojunction (24 $m^2\ g^{-1}$) showed enhanced light absorption, larger surface area, and suppressed charge recombination; efficiently reduced mono-, di-, and tri-nitrophenols to aminophenols under visible light/$NaBH_4$	[37]
Yadav et al./2025	Mn_3O_4/TiO_2-infused hydroxyapatite catalyst	2,4,6-Trinitrophenol	Mn_3O_4/TiO_2 on fish scale–derived HAp achieved 94.39% TNP reduction ($k = 0.1625\ min^{-1}$, 15 min); stable, reusable, low-cost, and sustainable via waste valorization	[38]

2962, 2026, 1, Downloaded from https://onlinelibrary.wiley.com/doi/10.1155/joch/1225741 by Sonia Mancipe Estevez - Cochrane Colombia , Wiley Online Library on [29/01/2026]. See the Terms and Conditions (https://onlinelibrary.wiley.com/terms-and-conditions) on Wiley Online Library for rules of use; OA articles are governed by the applicable Creative Commons License

once hydrolyzed was adjusted to 9.5 with a 2 M solution of $NaOH/Na_2CO_3$ (Macron Fine Chemicals 98%/Loba Chemie 98%). The suspension was left to age for 36 h at 160°C to ensure the formation of the laminas and finally the support was washed several times with distilled water and dried at 80°C overnight; the dried material was macerated in an agate mortar until fine and homogeneous powders were obtained giving rise to the formation of MgAl-HT.

The solid MgAl-HT was impregnated with NiO with different percentages by weight of the metal oxide (1, 3, 5, and 10 wt.%). The support was left stirring in a beaker at 300 rpm with the nickel precursor for 4 h. The impregnated solids were dried at 80°C for 6 h and macerated to obtain homogeneous powders. The materials were labeled NiO/MgAl 1%, NiO/MgAl 3%, NiO/MgAl 5%, and NiO/MgAl 10%.

2.2 | Characterization of Solids

The materials obtained were characterized to determine the structural, textural, spectroscopic, and compositional properties. X-Ray diffraction (XRD) was performed in a Rigaku MiniFlex II diffractometer with Cu Kα radiation, in a range of 10°–90° and with a step increment of 0.05° in 2θ using a counting time of one second. The textural analysis was performed using a Micromeritics ASAP 2020 instrument. Before analysis, the samples were degassed under vacuum (10^{-3} mmHg) at 100°C for 16 h to remove adsorbed surface molecules. The FTIR was performed in a Thermo Scientific Nicolet iS10 equipment with an ATR cell; the spectra were recorded in a wave number of 4000 to 400 cm^{-1} with a nominal resolution of 8 cm^{-1}Ultraviolet-visible diffuse reflectance spectroscopy (UV-Vis DRS) measurements were carried out on a Varian Cary 100 spectrophotometer equipped with an integrating sphere. The band gap energy was determined by identifying the maximum absorption band of each material and extrapolating the *X*-axis to the point where $Y = 0$, thereby obtaining the energies at which absorption occurs in the material. The band gap energy was determined by taking the maximum absorption band of each material and extrapolating to the *x*-axis considering $y = 0$. The XPS was made with a JEOL JPS-9200 instrument equipped with a Mg Kα radiation source (1253.6 eV). The XPS was operated at an energy of 10 eV with an X-ray power of 300 W. The displacement for charge correction was done by adjusting the spectrum with the 284.6 eV position of the carbon C 1 s.

2.3 | Photocatalytic Activity

The monitoring of the photocatalytic reaction in the reduction of nitroaromatic compounds was carried out in a glass reactor with a cooling jacket, 200 mL of a 10-ppm solution of the pollutant of 2,4-DNP (Sigma-Aldrich 98%) or 2,4,6-TNP (Sigma-Aldrich 98%), and 200 mg of Na_2SO_3 (Sigma-Aldrich 98%) as a sacrificial agent and 50 mg of catalyst was used and stirred at 800 rpm. Initially, the mixture was left stirring without exposure to UV light to ensure adsorption–desorption equilibrium for 30 min. Then, the suspension was irradiated with a Pen-Ray lamp with UV radiation of 254 nm and aliquots were taken every half hour until reaching 3 h of reaction. The samples were analyzed in a Thermo Fisher Scientific spectrophotometer at a wavelength from 190 to 500 nm, to verify the photocatalytic reduction reaction and the formation of the new product.

3 | Results and Discussion

3.1 | XRD

The crystallinity of the NiO/MgAl materials (1 wt.%, 3 wt.%, 5 wt.%, and 10 wt.%), along with the support, was assessed by XRD. The resulting diffraction patterns are presented in Figure 1. As can be seen, all the samples exhibited reflection peaks in 2θ characteristics of hydrotalcite-type materials (Ref. Pattern 22-0700, JCPDS) with signals strong (003), (006), (009), (110), and (113) and reflections a little more broadened in (015) and (018) planes [39]. The peaks recorded (111)∗ and (200)∗ at 2θ angles of 37° and 43.1°, respectively, correspond to the cubic structure of NiO (Ref. Pattern 47-1049, JCPDS) [40]. The sharp signal in the (003) plane shows the formation of highly crystalline solids [41]. The peak at $2\theta = 60°$ does not show any shift in position, which confirms that the compaction of the crystal lattice is preserved [42]. A hydromagnesite phase can be found in the XRD patterns [43, 44]; this phase might be due to precipitation before the complete formation of the hydrotalcite.

The lattice parameters, *a* and *c*, were determined from reflections (110) and (003), respectively, as $a = 2d_{(110)}$ and $c = 3d_{(003)}$. These lattice parameters are associated with the distance between the metal cations ($d_{(110)}$) and the interlaminar distance or basal space ($d_{(003)}$). The *a* parameter can vary depending on the ionic radius within the brucite-type structure, while the *c* parameter is influenced by the exchangeable anion present in the interlayer region [45]. According to the data shown in Table 2, the lattice parameters *a* and *c* are at values between 3 and 23 Å, respectively, showing a good fit to hydrotalcite-type materials in which the carbonate ion is present in the interlaminar region [46].

The *a* lattice parameter remains unchanged for both the MgAl-HT support and the NiO/MgAl solids, which suggests that the distance between cations remains, and in the brucite-like structure, the divalent and trivalent cations of Mg^{2+} and Al^{3+} are present. Similarly, it is observed that the *c* parameter does not

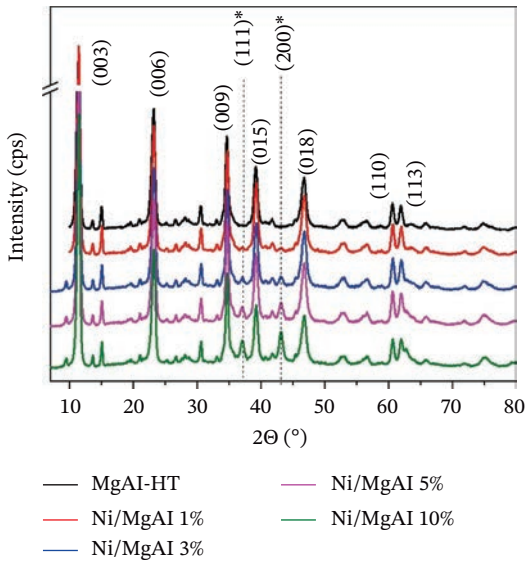


FIGURE 1 | X-Ray diffraction patterns of hydrotalcite MgAl-HT, NiO/MgAl 1 wt.%, 3 wt.%, 5 wt.%, and 10 wt.%. Hydromagnesite $Mg_5(CO_3)_4(OH)_2.4H_2O$.

2962, 2026, 1, Downloaded from https://onlinelibrary.wiley.com/doi/10.1155/joch/1225741 by Sonia Mancipe Estevez - Cochrane Colombia , Wiley Online Library on [29/01/2026]. See the Terms and Conditions (https://onlinelibrary.wiley.com/terms-and-conditions) on Wiley Online Library for rules of use; OA articles are governed by the applicable Creative Commons License

TABLE 2 | Crystallite size and lattice parameters for synthesized materials.

Solid	Lattice parameters		Crystallite size (nm) hydrotalcite	Crystallite size (nm) NiO $d_{(200)*}$
	a (nm)	*c* (nm)		
MgAl-HT	0.305	2.3165	13.32	—
NiO/MgAl 1%	0.305	2.3156	13.42	12.13
NiO/MgAl 3%	0.305	2.3063	12.92	12.95
NiO/MgAl 5%	0.305	2.3059	11.05	11.99
NiO/MgAl 10%	0.305	2.3078	9.43	11.66

present a modification, which suggests that the carbonate ions remain in the interlaminar region.

The crystal size was determined using the Debye–Scherrer equation; the values obtained for the planes characteristic of lamellar materials and for NiO in the (200)∗ specific plane are shown in Table 2. The average crystallite size for the hydrotalcite signals shows a small decrease in the solids with 3%, 5%, and 10% of NiO compared with the support. The decrease in crystallite size is related to the lower crystallinity that occurs in materials with higher NiO content [47]. The higher nucleation rate compared to the crystal growth rate could be responsible for the low crystallinity [48]. In the case of the NiO/MgAl photocatalysts, it is observed that the crystallite sizes measured in the (200)∗ plane for NiO are similar in each of the materials, possibly due to the impregnation synthesis method.

3.2 | Fourier Transform Infrared Spectroscopy (FTIR)

In Figure 2, the FTIR spectra of the NiO/MgAl show the different signals of the characteristic functional groups of hydrotalcite-type materials. A vibration band, centered at 3485 cm^{-1}, is assigned to the stretching and deformation vibrations of the -OH groups present in the brucite-type layers [49]. A shoulder of about 3030 cm^{-1} is evidenced in all the materials, due to the interaction of the H_2O of the intermediate layer and the carbonate ions [50]. The vibration bands at 1502 cm^{-1} are attributed to the antisymmetric stretching vibrations of the O–C–O bonds or the adsorption of free monodentate CO_3^{2-}species. These CO_3^{2-} species also present two bands of weak out-of-plane vibration with symmetry $\upsilon 1$ and $\upsilon 4$, approximately at 1366 and 669 cm^{-1}, respectively [51, 52]. The band at 1650 cm^{-1} was assigned to the –OH deformation mode of the water molecules in the interlaminar region [53]. All materials present a vibration band at 771 cm^{-1}, which is characteristic of the vibrational mode of the Al–OH interaction [54]. On the other hand, nickel oxide presents vibrations between 700 and 400 cm^{-1}, vibrations typical of the M-O bonds, centered at 565 cm^{-1}. Another band at 553 cm^{-1} is characteristic of the vibration modes of the hydroxyl groups influenced by the trivalent metal [41].

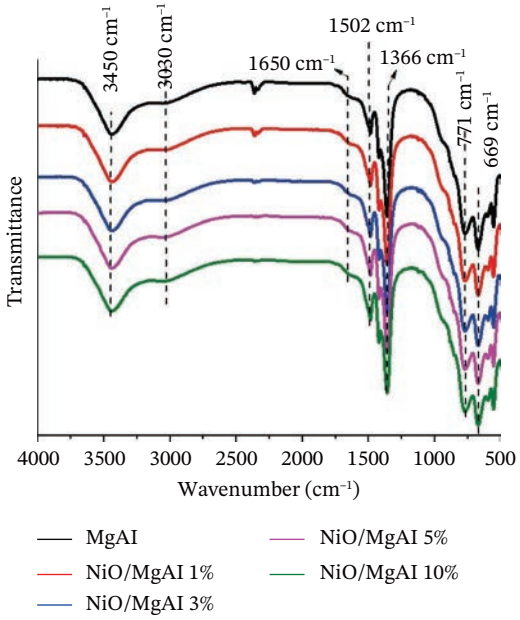


FIGURE 2 | FTIR spectra of the synthesized solids of MgAl-HT, NiO/MgAl with 1 wt.%, 3 wt.%, 5 wt.%, and 10 wt.%.

3.3 | Physisorption Analysis

Figure 3 shows the adsorption–desorption isotherms of N_2 of the materials studied. The adsorption–desorption isotherms of NiO/MgAl with 1 wt.%, 3 wt.%, 5 wt.%, and 10 wt.%. of the semiconductor correspond to type IV isotherms characteristic of mesoporous materials with a hysteresis loop H3 typical of laminar solids or in the form of slit according with the IUPAC classification [55]. As seen in Figure 3, the closing point of the hysteresis loops and the porosity of the materials remained relatively unchanged, implying a similarity in texture in all samples.

Table 3 shows the specific surface area, pore volume, and pore size distribution of the catalysts. Based on the reported data, it can be confirmed that the solids are mesoporous materials, with pore sizes ranging from 2 to 50 nm [56]. In addition, this result suggests that the addition of NiO does not increase the pore size. Therefore, a decrease in the specific surface area and the pore volume is not generated [49]. The latter remains unaffected by the increase in semiconductor content, with all materials exhibiting values around 0.11–0.13 cm^3/g. In Table 3, it is possible to observe that there is no modification in the distribution of the pore size and in the specific surface area, which may be because there is no presence of agglomerations in the samples after impregnation compared to the NiO precursor [57]. The hydrotalcite-type materials present a high dispersion of the divalent and trivalent metals in the brucite-type laminar, in this case, Mg^{2+} and Al^{3+}, respectively. This orderly and uniform structure allows in some way a uniform dispersion of the active species as NiO [58].

3.4 | UV-Vis DRS

The UV-Vis DRS spectra were evaluated to determine the radiation absorption threshold and the optical properties of the materials. Figure 4 shows the UV-Vis DRS spectra of the NiO/MgAl materials with 1 wt.%, 3 wt.%, 5 wt.%, and 10 wt.%, showing

2962, 2026, 1, Downloaded from https://onlinelibrary.wiley.com/doi/10.1155/joch/1225741 by Sonia Mancipe Estevez - Cochrane Colombia , Wiley Online Library on [29/01/2026]. See the Terms and Conditions (https://onlinelibrary.wiley.com/terms-and-conditions) on Wiley Online Library for rules of use; OA articles are governed by the applicable Creative Commons License

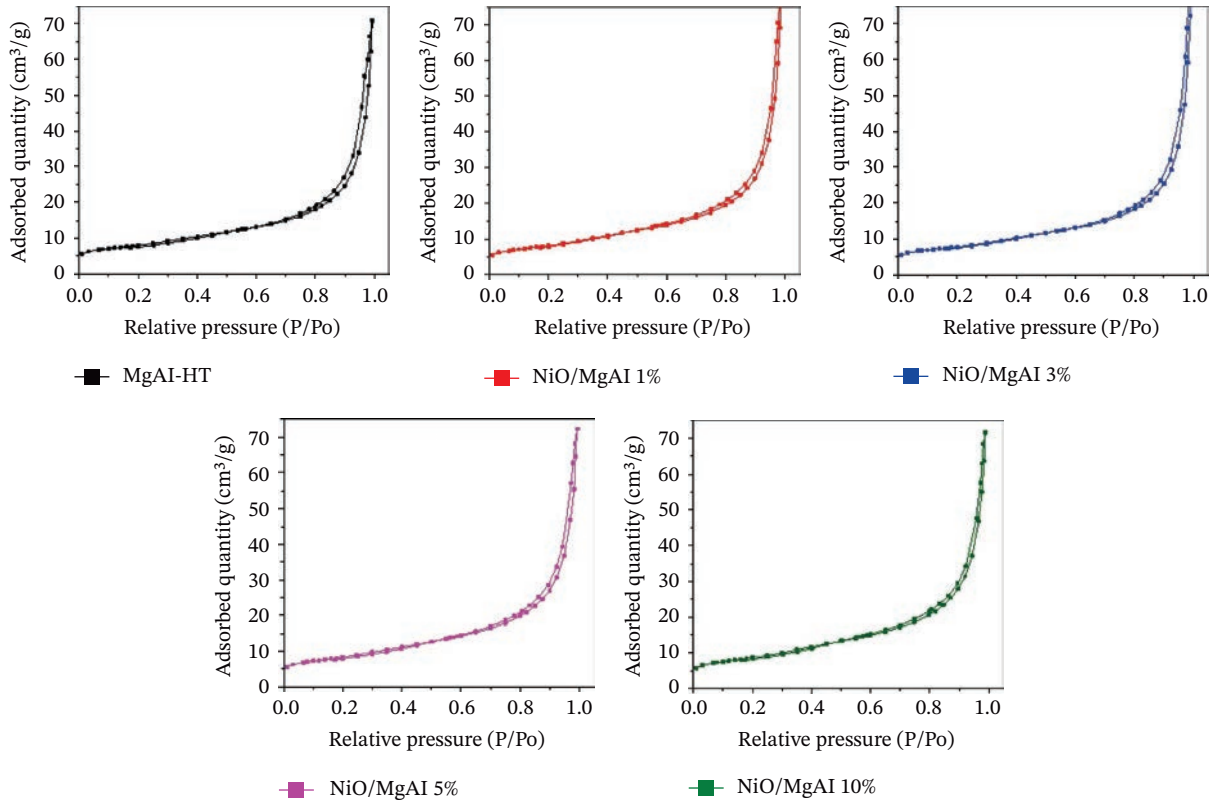


FIGURE 3 | Nitrogen adsorption–desorption isotherms of MgAl-HT, NiO/MgAl with 1 wt.%, 3 wt.%, 5 wt.%, and 10 wt.% of the semiconductor.

a broad absorption band in the wavelength range between 190 and 350 nm, which indicates that the materials have photoabsorption properties. It is observed that as the NiO content in hydrotalcite increases, the signal intensity also rises, likely due to greater photon absorption in the material [59]. The presence of NiO causes light absorption to begin around 350 nm, in contrast to MgAl-HT. Furthermore, it can be seen that the NiO/MgAl solids show a similar spectral profile. This behavior may be due to a possible coating of the MgAl support with NiO particles, which acts as an optical filter [60].

Besides, as can be seen in Table 3, as the content of NiO in the material increases, the bandgap energy (Eg) does not vary greatly due to the surface coating of MgAl-HT by NiO [61]. The addition of nickel oxide to hydrotalcite causes a slight decrease in the Eg, being lower for NiO/MgAl at 1 wt.% and 10 wt.% (4.73 and 4.78 eV, respectively). This decrease in this property could be related to a greater ease in the passage of electrons from the VB to the CB, which could favor the photocatalytic reduction reaction.

The correlation between NiO content and the band gap observed in the UV-Vis DRS spectra can be attributed to the introduction of Ni^{2+}-related states within the electronic structure of the MgAl-HT support. At low NiO loadings (NiO/MgAl 1%), well-dispersed Ni^{2+} ions interact with the host lattice, generating interfacial charge transfer states and defect levels that reduce the optical band gap from 5.41 to 4.73 eV. This effect enhances photon absorption at longer wavelengths (closer to 254 nm UV-C excitation with Pen-Ray lamp with UV radiation of 254 nm), which in turn improves photocatalytic activity. However, as the NiO content increases (NiO/MgAl 3%–5%), the band gap tends to widen again (≈5.06–5.18 eV). This behavior can be explained by partial aggregation of NiO clusters, which reduces the effective electronic interaction with the MgAl matrix and limits the density of defect states that contribute to band gap narrowing. At higher loadings (NiO/MgAl 10%), the band gap narrows once more (4.78 eV), most likely due to the predominance of bulk-like NiO domains that reintroduce localized states near the CB edge. Nevertheless, these larger NiO clusters simultaneously act as recombination centers, which counterbalances the optical

TABLE 3 | Experimental data of the textural and spectroscopic properties of MgAl-HT and NiO/MgAl materials.

Photocatalysts	Specific surface area S_{BET} (m^2/g)	Pore volume (cm^3/g)	Pore size distribution (nm)	Eg (eV)
MgAl-HT	28	0.11	15.43	5.41
NiO/MgAl 1%	29	0.12	15.05	4.73
NiO/MgAl 3%	27	0.13	17.55	5.18
NiO/MgAl 5%	30	0.11	13.99	5.06
NiO/MgAl 10%	31	0.11	13.32	4.78

2962, 2026, 1, Downloaded from https://onlinelibrary.wiley.com/doi/10.1155/joch/1225741 by Sonia Mancipe Estevez - Cochrane Colombia , Wiley Online Library on [29/01/2026]. See the Terms and Conditions (https://onlinelibrary.wiley.com/terms-and-conditions) on Wiley Online Library for rules of use; OA articles are governed by the applicable Creative Commons License

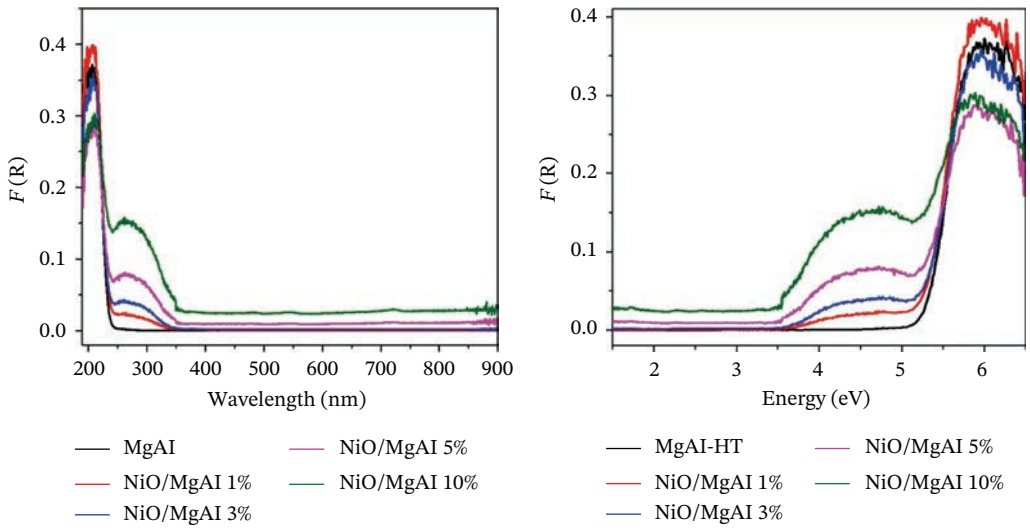


FIGURE 4 | UV-Vis diffuse reflectance spectrum of MgAl-HT, NiO/MgAl solids in wavelength and energy.

benefit and diminishes photocatalytic efficiency. Therefore, the UV-Vis DRS results indicate that the degree of band gap narrowing is not linear with NiO content, but rather depends on the dispersion–aggregation balance of NiO species on the MgAl surface.

The higher Eg values (5.41–4.73 eV) compared to bulk NiO and MgAl hydrotalcites arise from a combination of nanostructuring, surface/interface effects, and methodological factors. In particular, crystallite size reduction, cation substitution, and reduced defect density can shift the absorption edge toward higher energies, yielding wider optical band gaps than those reported for the bulk reference phases.

3.5 | X-Ray Photoelectron Spectroscopy (XPS)

The XPS analysis shows that the BE of Al 2p appears at 74.2 eV, corresponding to the aluminum hydroxides present in the brucite-type lamellar with an octahedral coordination [41]. In the case of Mg 2p, the signal at 50 eV corresponds to magnesium hydroxides.

Figure 5 shows the Ni 2p XPS spectra of the solids of NiO/MgAl at 3 wt.%, 5 wt.%, and 10 wt.% Ni surface species which were not detected in NiO/MgAl 1%. The signal of Ni $2p_{3/2}$ at about 855.8 eV could be attributed to NiO with a satellite peak at ~861 eV. NiOOH surface species appear at 857 eV in the catalyst with the highest loading of NiO. The formation of nickel oxyhydroxide has been associated with the spectra O1s (did not show).

The photocatalytic behavior of the synthesized NiO/MgAl materials is closely related to their band structure. The VB position of the photocatalysts was determined by XPS, obtaining the corresponding values for the four Ni-containing solids and for the MgAl support, as shown in Table 4. Similarly, the CB position was calculated using the equation: $E_{CB} = E_{VB} - Eg$.

The VB value for the MgAl support was 2.24 eV, which is consistent with that reported by Piña-Pérez et al. [62]. After the incorporation of nickel, this value decreased, probably due to the insertion of the metal into the support structure. Based on these results, a band structure diagram was constructed for the materials, also including the HOMO and LUMO energy levels of the studied organic molecules (Table 4).

According to this diagram (Figure 6(a)), a higher adsorption capacity of the contaminant species can be inferred for the NiO/MgAl 1% photocatalyst, since its VB is closer to the LUMO level of the 2,4-DNP and 2,4,6-TNP molecules (Figure 6(b)). This suggests that this material exhibits a more favorable behavior for the reduction of organic pollutant compounds.

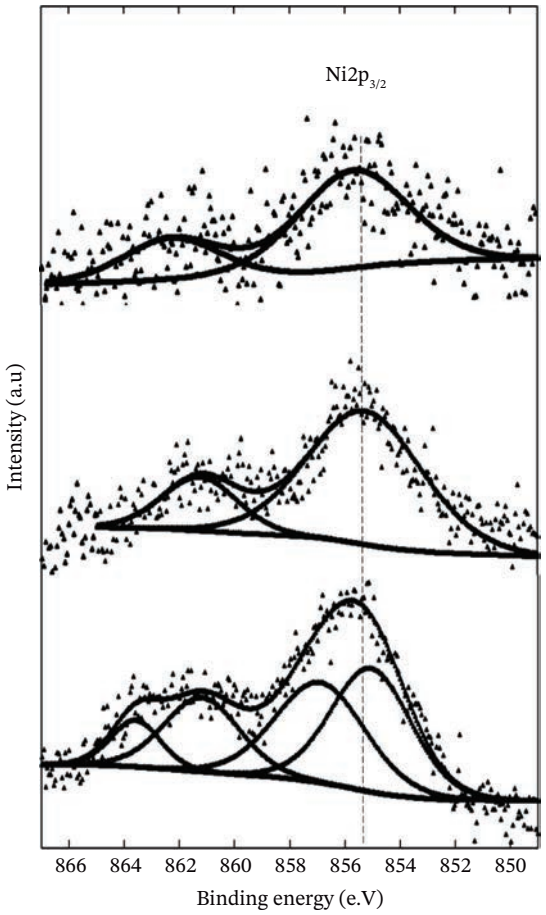


FIGURE 5 | Ni 2p XPS spectra of the solids of NiO/MgAl at 3 wt.%, 5 wt.%, and 10 wt.%.

2962, 2026, 1, Downloaded from https://onlinelibrary.wiley.com/doi/10.1155/joch/1225741 by Sonia Mancipe Estevez - Cochrane Colombia , Wiley Online Library on [29/01/2026]. See the Terms and Conditions (https://onlinelibrary.wiley.com/terms-and-conditions) on Wiley Online Library for rules of use; OA articles are governed by the applicable Creative Commons License

TABLE 4 | Values of Eg, VB, and CB of material.

Photocatalysts	Eg (eV)	VB (eV)	CB (eV)	2,4-DNP (eV)		2,4,6-TNP (eV)	
MgAl-HT	5.41	**2.24**	**−3.17**	LUMO	HOMO	LUMO	HOMO
NiO/MgAl 1%	4.73	**1.51**	**−3.22**				
NiO/MgAl 3%	5.18	**1.73**	**−3.45**	−10,517	0.129	−11,367	−0.640
NiO/MgAl 5%	5.06	**2.3**	**−3.3**				
NiO/MgAl 10%	4.78	**1.7**	**−3.08**				

Note: Values of Eg, valence band (VB), and conduction band (CB) of materials.
Abbreviations: CB, conduction band; VB, valence band.

3.6 | Evaluation of the Photocatalytic Activity

The progress of the photocatalytic reduction of nitroaromatic compounds under UV irradiation was monitored using UV–Vis spectrophotometry, scanning in the range of 200–500 nm. The maximum absorption wavelengths of 2,4,6-TNP and 2,4-DNP were identified at 354 and 357 nm, respectively. In reduction reactions, the pH of the solution plays a crucial role, as it influences the chemical form of the nitroaromatic compounds. The feasibility of electron transfer is strongly influenced by the pH of the solution. Nitrophenol remains stable under acidic conditions, with measured pH values of 4.38 for 2,4-DNP and 4.549 for 2,4,6-TNP. Under alkaline conditions, however, the formation of the nitrophenolate ion intermediate is favored. This species arises from the deprotonation of nitrophenols in basic media, and its formation is further promoted by the addition of Na_2SO_3. After introducing this sacrificial agent, the pH increased to 9.39 for 2,4-DNP and 8.83 for 2,4,6-TNP. It is also noteworthy that LDHs are inherently basic materials; consequently, upon addition of the NiO/MgAl 1% photocatalyst, the pH rose slightly further to 10.043 and 10.019 for 2,4-DNP and 2,4,6-TNP, respectively, and remained stable throughout the reaction. For both DNP and TNP reactions, the absorption spectra exhibit a band in the 200–250 nm range (Figure 7) which can be attributed to the presence of sulfite ions (SO_3^{2-}) [63] as well as $\pi \longrightarrow \pi*$ transitions of the aromatic groups [64].

The absorption bands that were followed in the course of the reaction were at 354 and 357 nm for 2.4,6-TNP and 2,4-DNP, respectively, considering that the reduction was carried out in the presence of the sacrificial agent Na_2SO_3, which allows the obtaining of the respective nitrophenolate ions.

In Figure 8, it can be seen that the bands at 357 and 354 nm for 2,4-DNP and 2,4,6-TNP, respectively, gradually decrease as the reaction time increases, showing a transformation of the reactants. In the case of TNP, it is observed that this decrease in the signal is accompanied by the appearance of a band close to 275 nm that corresponds to the formation of the respective aminophenol, obtained from the photocatalytic reduction of TNP. In addition, in the reduction of TNP, two isosbestic points around 280 and 313 nm are evidenced, which indicate the equilibrium between the reagent and the product, suggesting the formation of the respective aminophenol as the only reaction product [65].

In the photocatalytic activity for the reduction of 2,4-DNP, a diminution in the band at 357 nm is observed, showing a decrease in the concentration of the contaminant. In the same way, at 30, 60, and 90 min of reaction, the formation of two signals around 260 and 424 nm is evident, which corroborate the formation of the 2,4-DNP ion in the solution. However, after 90 min, these signals decrease as the reaction progresses, confirming the reduction of the contaminant [35]. The formation of diaminophenol was confirmed at 303 nm, with a slight increase in the signal at this wavelength. Furthermore, the presence of 2-amino-4-nitrophenol as an intermediate can be ruled out, since its characteristic signals at 248.50, 355.94, and 383.71 nm are not observed [66].

The monitoring of photocatalytic activity using UV-Vis spectroscopy allowed for the evaluation of the reduction of substituted nitroaromatic compounds (Figure 9). During the reactions, an initial period of 30 min was observed, during which the adsorption–desorption equilibrium was established in the absence of UV radiation. In this phase, a greater decrease in concentration was evident when using

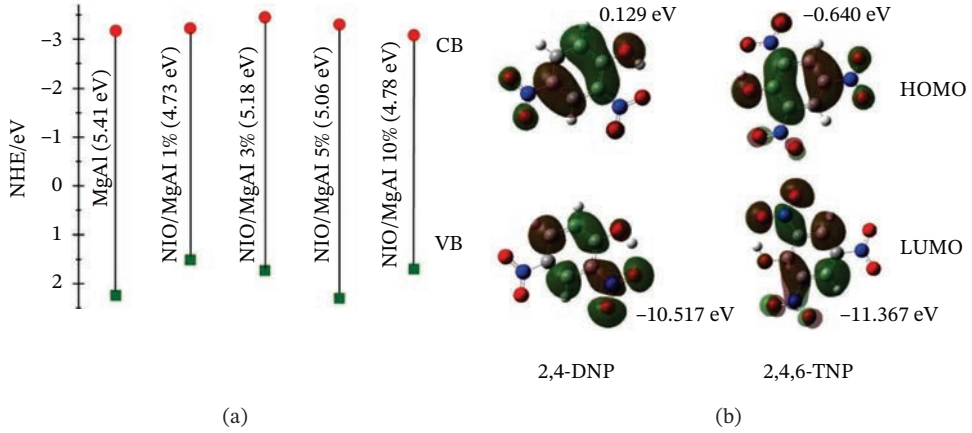


FIGURE 6 | (a) Band structures diagram; (b) schematic diagram of LUMO and HOMO of 2,4-DNP and 2,4,6-TNP.

2962, 2026, 1, Downloaded from https://onlinelibrary.wiley.com/doi/10.1155/joch/1225741 by Sonia Mancipe Estevez - Cochrane Colombia , Wiley Online Library on [29/01/2026]. See the Terms and Conditions (https://onlinelibrary.wiley.com/terms-and-conditions) on Wiley Online Library for rules of use; OA articles are governed by the applicable Creative Commons License

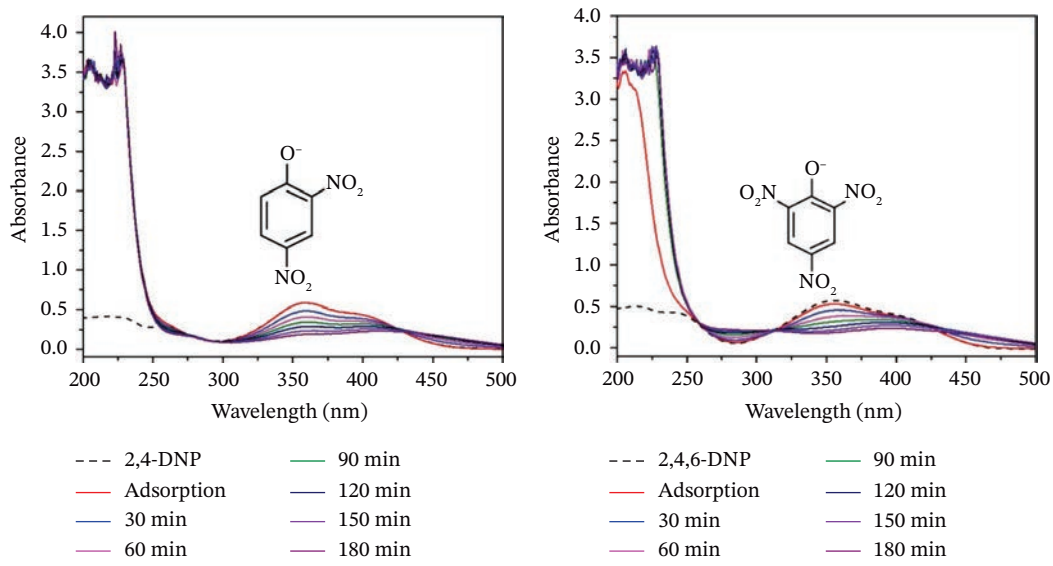


FIGURE 7 | UV-Vis absorption spectra of dinitro- and trinitrophenol used NiO/MgAl 1%.

the NiO/MgAl 1% catalyst. After the adsorption period, the Pen-Ray lamp was turned on, initiating the photocatalytic activity. In the case of 2,4-DNP reduction, the NiO/MgAl 3% and 10% catalysts exhibited similar activity, while the NiO/MgAl 5% catalyst showed the lowest reduction. The most active photocatalyst for the reduction of 2,4-DNP was the NiO/MgAl 1% material.

The reduction of 2,4,6-TNP indicates that photolysis does not lead to a decrease in pollutant concentration; instead, an increase in relative concentration is observed. This apparent increase may be attributed to the formation of intermediate products rather than the actual reduction of TNP. The NiO/MgAl solids with 1 wt.% and 3 wt.% exhibit the highest photocatalytic reduction of TNP. It can be inferred that the superior activity of the 1% semiconductor material in the photocatalytic reduction of both 2,4-DNP and TNP is due to its lower Eg.

To compare and evaluate the efficiency of the photocatalytic reduction system of 2,4,6-TNP, three reactions were carried out. Figure 10(a) shows the reaction using only the NiO/MgAl 1% catalyst. In this case, it is observed that the presence of the photocatalytic material promotes the degradation of the compound but not its reduction. This is evidenced by the decrease in the absorption band at 354 nm, without the appearance of isosbestic points or an increase in the signal at 275 nm. Additionally, the signal around 200 nm also decreases, confirming that the predominant process is the degradation of 2,4,6-TNP.

In the case of Figure 10(b), the reduction reaction was carried out using only Na_2SO_3. Although a partial reduction of the target compound is observed, the efficiency of the process significantly improves when both the catalyst and the sacrificial agent are added.

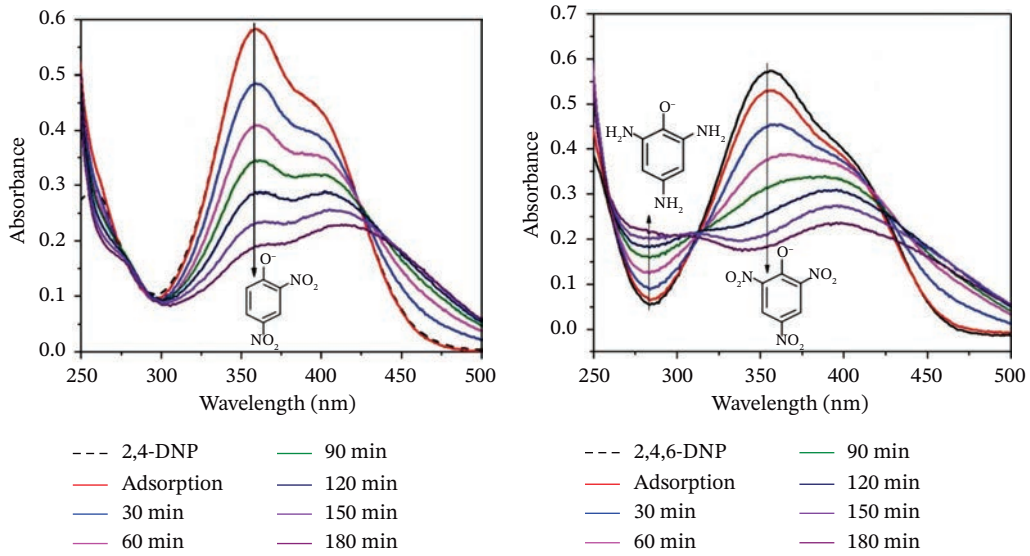


FIGURE 8 | Progress of reduction reaction of 2,4-DNP and 2,4,6-TNP using NiO/MgAl 1% as photocatalysts.

2962, 2026, 1, Downloaded from https://onlinelibrary.wiley.com/doi/10.1155/joch/1225741 by Sonia Mancipe Estevez - Cochrane Colombia , Wiley Online Library on [29/01/2026]. See the Terms and Conditions (https://onlinelibrary.wiley.com/terms-and-conditions) on Wiley Online Library for rules of use; OA articles are governed by the applicable Creative Commons License

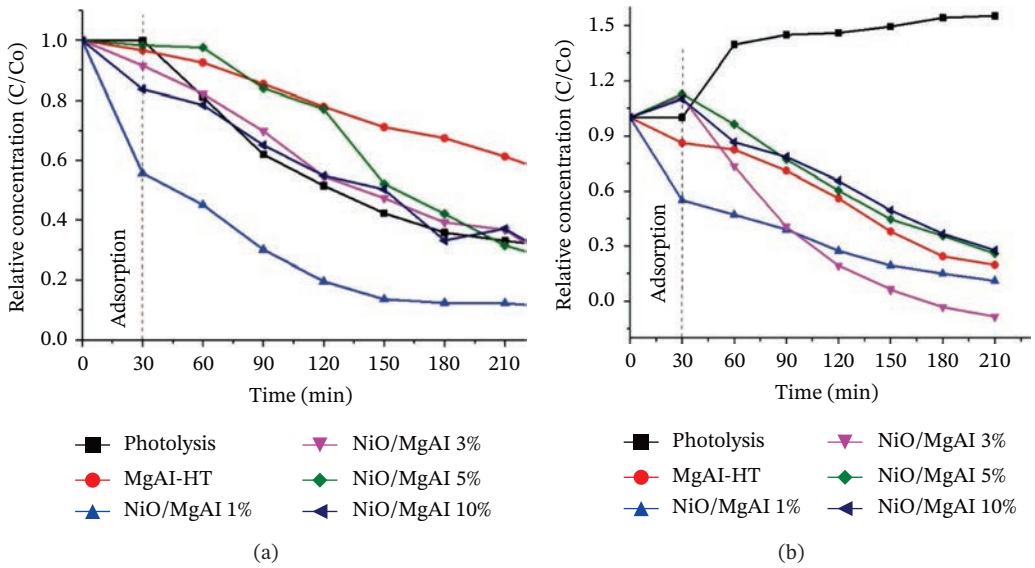


FIGURE 9 | Photocatalytic activity of the synthesized materials in the reduction of (a) 2,4-dinitrophenol and (b) 2,4,6-trinitrophenol.

In Figure 10(c), the reaction is shown using sodium bromate ($NaBrO_3$) as an electron scavenger. In this case, the presence of the sacrificial agent inhibits the reduction reaction, as it prevents the photogenerated electrons from participating in the formation of aminophenol. Additionally, the simultaneous presence of Na_2SO_3 prevents degradation from occurring through the photogenerated holes. This final reaction confirms that the reduction of 2,4,6-TNP indeed proceeds via photogenerated electrons.

To evaluate the efficiency of the photocatalysts, a kinetic study was carried out using the following equation:

$$\ln\left(\frac{C_0}{C_t}\right) = -Kt, \tag{1}$$

where C_0 and C_t are the concentrations of DNP and TNP at time zero and at time t. Furthermore, from the plot of $\ln(C_0/C_t)$ versus time, it can be concluded that the photoreduction of reactants follows pseudo-first-order reaction kinetics. The rate constant (k, in min^{-1}) was determined from the plot. Notably, the NiO/MgAl 1% material exhibits a rate constant of 0.0129 min^{-1} for 2,4-DNP photoreduction and 0.010 min^{-1} for TNP photoreduction. In the case of TNP, the NiO/MgAl 3% catalyst also shows a good R^2 fit and a high rate constant. However, considering that the reduction percentages for the 1% and 3% solids are 80.75% and 93.73%, respectively, the two best values are relatively close (Table 5).

It is important to note that photoreduction involves two processes. First, in a basic medium, after the addition of Na_2SO_3, the phenolate ion is formed. In the second step, this phenolate ion is

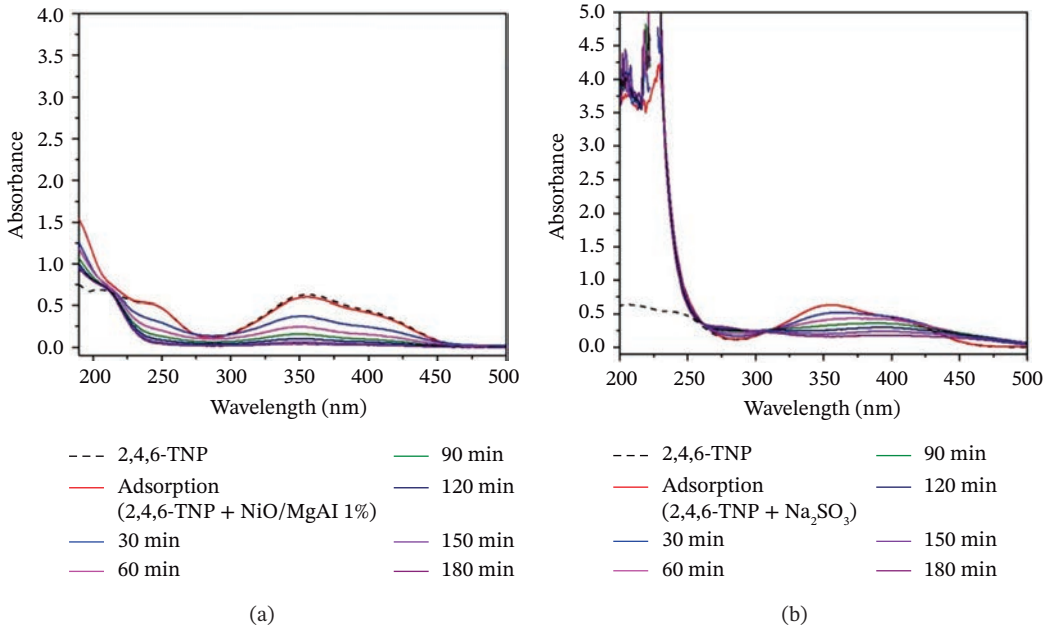


FIGURE 10 | (Continued)

2962, 2026, 1, Downloaded from https://onlinelibrary.wiley.com/doi/10.1155/joch/1225741 by Sonia Mancipe Estevez - Cochrane Colombia , Wiley Online Library on [29/01/2026]. See the Terms and Conditions (https://onlinelibrary.wiley.com/terms-and-conditions) on Wiley Online Library for rules of use; OA articles are governed by the applicable Creative Commons License

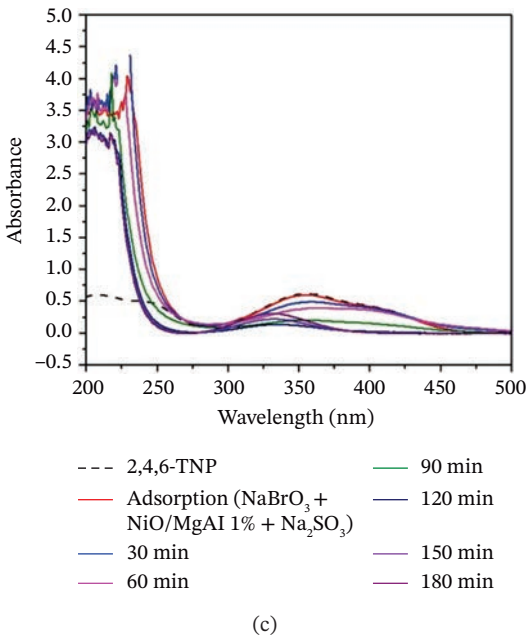


FIGURE 10 | Evaluation of the reduction of 2,4,6-trinitrophenol using (a) only NiO/MgAl 1%, (b) only Na_2SO_3, and (c) $NaBrO_3$, Na_2SO_3, and NiO/MgAl 1%.

converted into aminophenol. According to the results presented in Table 5, which compares the percentage reduction and rate constant using the NiO/MgAl 1% material, the reduction follows the trend DNP > TNP. Additionally, the rate constant in photoreduction decreases as the number of -NO_2 substituents increases, which can be attributed to molecular hindrance and the steric effect of these substituents [67].

According to Soumaya and colleagues [71], although $NaBH_4$ is a strong reducing agent in aqueous media, its exclusive use in the reduction of 2,4,6-TNP to 2,4,6-TAP remains inefficient, as the reaction progresses slowly due to kinetic barriers. Furthermore, $NaBH_4$ poses additional drawbacks when compared to Na_2SO_3, including the potential generation of toxic boron-containing byproducts [72, 73], lower photostability, stringent requirements for pH and temperature control [74], higher cost, and restricted availability. For this reason, the present study represents a valuable contribution to the field of photocatalytic reduction of 2,4-DNP and 2,4,6-TNP, by highlighting the potential of Na_2SO_3 as an efficient, easy-to-handle, and environmentally safer reducing agent, positioning it as a viable alternative for sustainable processes of remediation and chemical transformation. Table 6 shows a comparative analysis of the reduction of nitrophenols using $NaBH_4$ as a reducing agent compared to the work presented that uses Na_2SO_3.

The representation of the photocatalytic reduction of 2,4-DNP in the presence of Na_2SO_3 can be observed in Figure 11.

The NiO semiconductor, supported and dispersed on MgAl hydrotalcite, facilitated the absorption of UV radiation from the Pen-Ray lamp, leading to the excitation of electrons from the VB to the CB. In this process, the photogenerated holes in the VB interact with sulfite ions (SO_3^{2-}), generating sulfite radicals ($SO_3^{\bullet-}$), while the excited electrons are transferred from the semiconductor to the pollutant molecule (nitro group), ultimately leading to the formation of aminophenols. The presence of the sacrificial agent (sodium sulfite) plays a crucial role in preventing the rapid recombination of charge

TABLE 5 | Kinetic parameters of photocatalytic activity of 2,4-dinitrophenol and 2,4,6-trinitrophenol.

Photocatalysts	Photoactivity (%)*		K (min^1)		R^2	
	2,4-DNP	2,4,6-TNP	2,4-DNP	2,4,6-TNP	2,4-DNP	2,4,6-TNP
Photolysis	63.57	—	7.51×10^{-3}	—	0.97	—
MgAl-HT	28.90	43.99	2.9×10^{-3}	6×10^{-3}	0.99	0.91
NiO/MgAl 1%	86.42	80.75	1.29×10^{-2}	1×10^{-2}	0.99	0.97
NiO/MgAl 3%	52.75	93.73	5.2×10^{-3}	1.9×10^{-2}	0.97	0.97
NiO/MgAl 5%	47.92	55.39	3.9×10^{-3}	5.8×10^{-3}	0.78	0.87
NiO/MgAl 10%	49.79	50.52	4.7×10^{-3}	4.9×10^{-3}	0.98	0.89

*Photocatalytic activity of reduction of 2,4-DNP and 2,4,6-TNP after 2 h of exposure to UV light.

2962, 2026, 1, Downloaded from https://onlinelibrary.wiley.com/doi/10.1155/joch/1225741 by Sonia Mancipe Estevez - Cochrane Colombia , Wiley Online Library on [29/01/2026]. See the Terms and Conditions (https://onlinelibrary.wiley.com/terms-and-conditions) on Wiley Online Library for rules of use; OA articles are governed by the applicable Creative Commons License

TABLE 6 | Comparative analysis of the reduction of nitrophenols.

Type of catalysts	Uses	Sacrificial agent	Rate constants K (min^1) or conversion (%)	Reference
AuNPs AgNPs	Reducing 2,4-dinitrophenol	$NaBH_4$	7.4×10^{-1} (rate constants) 4.8×10^{-1} (rate constants)	[35]
NH_2-MIL-101(Cr)	Adsorption	—	0.26458542 mg/g/min (rate constants)	[68]
MOEAgNPs DREAgNPs	Reducing 2,4-dinitrophenol	$NaBH_4$	4.2×10^{-2} (rate constants) 2.6×10^{-2} (rate constants)	[69]
ZnO NSs/CuO NPs	Reducing 2,4-dinitrophenol Reducing 2,4,6-trinitrophenol	$NaBH_4$	1.14 (rate constants) 0.95 (rate constants)	[70]
In_2S_3/Ni-MOF	Photocatalytic hydrogenation of 2,4,6-trinitrophenol	$NaBH_4$	96.31% (conversion)	[71]
Ag@Ru/TiO_2	Reducing 2,4-dinitrophenol Reducing 2,4,6-trinitrophenol	$NaBH_4$	100% (conversion) 100% (conversion)	[67]
NiO/MgAl 1%	Reducing 2,4-dinitrophenol Reducing 2,4,6-trinitrophenol	Na_2SO_3	1.29×10^{-2} (rate constants) 1×10^{-2} (rate constants)	This work

2962, 2026, 1, Downloaded from https://onlinelibrary.wiley.com/doi/10.1155/joch/1225741 by Sonia Mancipe Esteves - Cochrane Colombia , Wiley Online Library on [29/01/2026]. See the Terms and Conditions (https://onlinelibrary.wiley.com/terms-and-conditions) on Wiley Online Library for rules of use; OA articles are governed by the applicable Creative Commons License

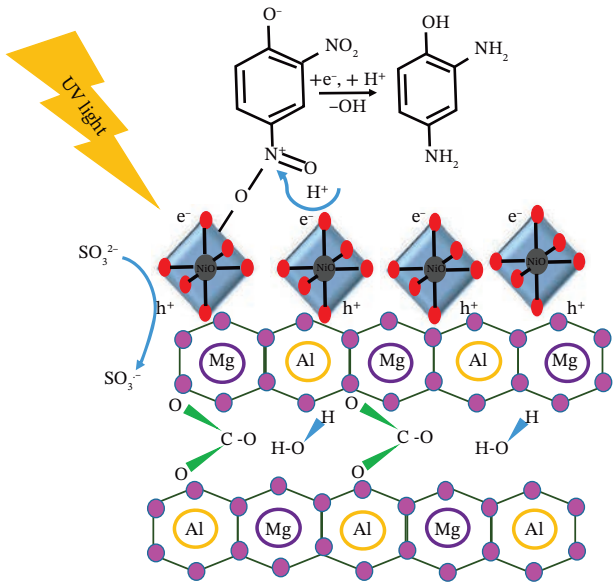


FIGURE 11 | Photocatalytic reduction mechanism of 2,4-dinitrophenol.

carriers (electron–hole pairs), enhancing the photocatalytic efficiency.

3.7 | Reuse of the Catalyst

Once the contaminant reduction reaction was evaluated, a reuse test of the NiO/MgAl 1 wt.% photocatalyst was carried out for the reduction of 2,4-DNP and 2,4,6-TNP over three cycles, in order to assess the stability of the material, as shown in Figure 12. After each reaction, the photocatalyst was recovered from the solution and subjected to thermal treatment at 80°C overnight. Subsequently, the resulting laminar material was added to a fresh solution of each contaminant, and the system was evaluated under the same conditions described in the experimental section. As observed, reduction efficiencies of 72% and 68% were achieved after the third reuse cycle for 2,4-DNP and 2,4,6-TNP, respectively. These results confirm that the solid containing 1 wt.% NiO exhibits good stability and can be considered a reusable and promising material for the photoreduction of nitroaromatic compounds.

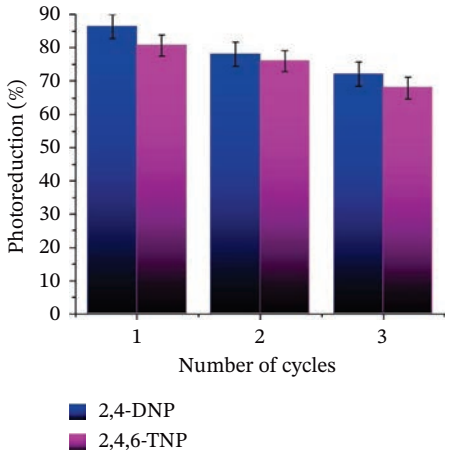


FIGURE 12 | Reusability of NiO/MgAl 1% photocatalyst in the reduction of nitroaromatic compounds.

4 | Conclusion

Structural characterization by XRD and FTIR confirmed that all materials preserved the hydrotalcite-like structure with high crystallinity, even after the incorporation of NiO, whose signals became evident from 3% loading onwards. Textural analysis showed a mesoporous type IV structure with H3 hysteresis typical of layered solids, with no significant changes in surface area or pore volume, indicating good dispersion of NiO. UV-Vis DRS spectra revealed enhanced UV absorption and a decrease in Eg, particularly for materials with 1% and 10% NiO, which favored photocatalytic activity. XPS analysis confirmed the presence of Ni^{2+} (NiO) and, at higher concentrations, the formation of NiOOH, suggesting complex interactions between the semiconductor and the lamellar support. Under UV irradiation, the photocatalytic reduction of dinitro- and trinitrophenol was most efficient with the 1% NiO/MgAl material, achieving 86.42% and 80.75% conversion, respectively, following pseudo-first-order kinetics.

Author Contributions

Conceptualization and methodology: Sonia Mancipe Estevez, José J. Martínez, Leimmy Calderon, Daniela Barrera, Dora Solis, and Francisco Tzompanzi. Experimental work and writing–original draft preparation: Leimmy Calderon, Daniela Barrera, José J. Martínez, Sonia Mancipe Estevez, Dora Solis, and Francisco Tzompanzi. Writing–review and editing: Hugo Rojas, Sonia Mancipe Estevez, José J. Martínez, and Claudia Castañeda. Supervision: José J. Martínez, Hugo Rojas, Sonia Mancipe Estevez, and Claudia Castañeda. Project administration: José J. Martínez and Sonia Mancipe Estevez.

Acknowledgments

The authors acknowledge Universidad Pedagógica y Tecnológica de Colombia and Vicerrectoria de Investigaciones-UPTC for the financial support.

Funding

No funding was received for this manuscript.

Conflicts of Interest

The authors declare no conflicts of interest.

Data Availability Statement

The data that support the findings of this study are available from the corresponding author upon reasonable request.

References

1. P. P. Mandvi, S. Ballal, M. Chahar, et al., "Construction of a 3D Flower-Like NiO/Mn3O4 Heterojunction Using Tulsi Leaf Extract for Enhanced Photodegradation of Thiamethoxam Pesticide and Organic Dyes Under Direct Sunlight," *Materials Advances* 5 (2024): 8097–8110, https://doi.org/10.1039/d4ma00708e.

2. I. Ibrahim, C. Athanasekou, G. Manolis, et al., "Photocatalysis as an Advanced Reduction Process (ARP): The Reduction of 4-Nitrophenol Using Titania Nanotubes-Ferrite Nanocomposites," *Journal of Hazardous Materials* 372 (2019): 37–44, https://doi.org/10.1016/j.jhazmat.2018.12.090.

2962, 2026, 1, Downloaded from https://onlinelibrary.wiley.com/doi/10.1155/joch/1225741 by Sonia Mancipe Estevez - Cochrane Colombia , Wiley Online Library on [29/01/2026]. See the Terms and Conditions (https://onlinelibrary.wiley.com/terms-and-conditions) on Wiley Online Library for rules of use; OA articles are governed by the applicable Creative Commons License

3. K.-S. Ju and R. E. Parales, "Nitroaromatic Compounds, From Synthesis to Biodegradation," *Microbiology and Molecular Biology Reviews* 74, no. 2 (2010): 250–272, https://doi.org/10.1128/MMBR.00006-10.

4. A. Al-Nafiey, A. Kumar, M. Kumar, et al., "Nickel Oxide Nanoparticles Grafted on Reduced Graphene Oxide (rGO/NiO) as Efficient Photocatalyst for Reduction of Nitroaromatics Under Visible Light Irradiation," *Journal of Photochemistry and Photobiology A: Chemistry* 336 (2017): 198–207, https://doi.org/10.1016/j.jphotochem.2016.12.023.

5. C. Castañeda, F. J. Tzompantzi, and R. Gomez, "Photocatalytic Reduction of 4-Nitrophenol on in Situ Fluorinated Sol–Gel TiO2 Under UV Irradiation Using Na2SO3 as Reducing Agent," *Journal of Sol-Gel Science and Technology* 80, no. 2 (2016): 426–435, https://doi.org/10.1007/s10971-016-4104-2.

6. I. Ivančev-Tumbas, R. Hobby, B. Küchle, S. Panglisch, and R. Gimbel, "p-Nitrophenol Removal by Combination of Powdered Activated Carbon Adsorption and Ultrafiltration–Comparison of Different Operational Modes," *Water Research* 42, no. 15 (2008): 4117–4124, https://doi.org/10.1016/j.watres.2008.07.009.

7. M. Bielska and J. Szymanowski, "Micellar Enhanced Ultrafiltration of Nitrobenzene and 4-Nitrophenol," *Journal of Membrane Science* 243, no. 1-2 (2004): 273–281, https://doi.org/10.1016/j.memsci.2004.06.030.

8. P. Sarkar and A. Dey, "4-Nitrophenol Biodegradation by an Isolated and Characterized Microbial Consortium and Statistical Optimization of Physicochemical Parameters by Taguchi Methodology," *Journal of Environmental Chemical Engineering* 8, no. 5 (2020): 104347, https://doi.org/10.1016/j.jece.2020.104347.

9. S. M. S. S, D. S. Vijayan, M. Anand, M. Ajona, and T. Jarin, "Biodegradation of P-Nitro Phenol Using a Novel Bacterium Achromobacter Denitrifacians Isolated From Industrial Effluent Water," *Water Science and Technology* 84, no. 10-11 (2021): 3334–3345, https://doi.org/10.2166/wst.2021.354.

10. N. Modirshahla, M. A. Behnajady, and S. Mohammadi-Aghdam, "Investigation of the Effect of Different Electrodes and Their Connections on the Removal Efficiency of 4-Nitrophenol From Aqueous Solution by Electrocoagulation," *Journal of Hazardous Materials* 154, no. 1-3 (2008): 778–786, https://doi.org/10.1016/j.jhazmat.2007.10.120.

11. S. Kumar, S. Singh, and V. C. Srivastava, "Electro-Oxidation of Nitrophenol by Ruthenium Oxide Coated Titanium Electrode: Parametric, Kinetic and Mechanistic Study," *Chemical Engineering Journal* 263 (2015): 135–143, https://doi.org/10.1016/j.cej.2014.11.051.

12. J.-M. Chern and Y.-W. Chien, "Adsorption of Nitrophenol Onto Activated Carbon: Isotherms and Breakthrough Curves," *Water Research* 36, no. 3 (2002): 647–655, https://doi.org/10.1016/S0043-1354(01)00258-5.

13. S. B. Haderlein and R. P. Schwarzenbach, "Adsorption of Substituted Nitrobenzenes and Nitrophenols to Mineral Surfaces," *Environmental Science and Technology* 27, no. 2 (1993): 316–326, https://doi.org/10.1021/es00039a012.

14. P. Cañizares, M. Díaz, J. A. Domínguez, J. García-Gómez, and M. A. Rodrigo, "Electrochemical Oxidation of Aqueous Phenol Wastes on Synthetic Diamond Thin-Film Electrodes," *Industrial & Engineering Chemistry Research* 41, no. 17 (2002): 4187–4194, https://doi.org/10.1021/ie0105526.

15. X. Liu, D. Gregurec, J. Irigoyen, et al., "Precise Localization of Metal Nanoparticles in Dendrimer Nanosnakes or Inner Periphery and Consequences in Catalysis," *Nature Communications* 7, no. 1 (2016): 13152, https://doi.org/10.1038/ncomms13152.

16. X. Chen, Y. Wang, X. Fan, G. Zhu, Y. Liu, and X. Quan, "Efficient Electro-Fenton Degradation of Organic Pollutants Via the Synergistic Effect of 1O2 and •OH Generated on Single FeN4 Sites," *Science of the Total Environment* 932 (2024): 173042, https://doi.org/10.1016/j.scitotenv.2024.173042.

17. S. Yuan, M. Tian, Y. Cui, L. Lin, and X. Lu, "Treatment of Nitrophenols by Cathode Reduction and Electro-Fenton Methods," *Journal of Hazardous Materials* 137, no. 1 (2006): 573–580, https://doi.org/10.1016/j.jhazmat.2006.02.069.

18. X. Qiao, K. Yu, J. Xu, et al., "Engineered Nanoscale Schwertmannites as Fenton–Like Catalysts for Highly Efficient Degradation of Nitrophenols," *Applied Surface Science* 548 (2021): 149248, https://doi.org/10.1016/j.apsusc.2021.149248.

19. Y. Chu, H. Su, R. Lv, and X. Zhang, "Enhanced Electro-Reduction of Fe3+ to Fe2+ by Acidified Carbon Nanotube-Modified Graphite Cathode and Its Application in a Novel Fenton Process for p-Nitrophenol Degradation," *Journal of Water Process Engineering* 40 (2021): 101912, https://doi.org/10.1016/j.jwpe.2020.101912.

20. N. Wang, G. Lv, L. He, and X. Sun, "New Insight Into Photodegradation Mechanisms, Kinetics and Health Effects of p-Nitrophenol by Ozonation in Polluted Water," *Journal of Hazardous Materials* 403 (2021): 123805, https://doi.org/10.1016/j.jhazmat.2020.123805.

21. Q. Liu, L. Zhou, L. Liu, et al., "Magnetic ZnO@Fe3O4 Composite for Self-Generated H2O2 Toward Photo-Fenton-Like Oxidation of Nitrophenol," *Composites Part B: Engineering* 200 (2020): 108345, https://doi.org/10.1016/j.compositesb.2020.108345.

22. M. Mishra, T. Urooj, A. Singh, and S. Pandey, "A New Approach for Synthesis of Bismuth Oxide Derived Photocatalyst for Degradation of Para Nitrophenol," *Desalination and Water Treatment* 319 (2024): 100558, https://doi.org/10.1016/j.dwt.2024.100558.

23. S. Pandey, A. Singh, A. Kumar, et al., "Photocatalytic Degradation of Noxious p-Nitrophenol Using Hydrothermally Synthesized Stannous and Zinc Oxide Catalysts," *Physics and Chemistry of the Earth, Parts A/B/C* 133 (2024): 103512, https://doi.org/10.1016/j.pce.2023.103512.

24. M. Mahajan, S. Kumar, J. Gaur, et al., "Role of Cellulose, Phenolic Compounds, and Water-Soluble Proteins in ZnO Nanoparticle Synthesis Using Mangifera Indica Leaf Extract for Photocatalytic and Antioxidant Investigations," *Colloids and Surfaces A: Physicochemical and Engineering Aspects* 720 (2025): 137066, https://doi.org/10.1016/j.colsurfa.2025.137066.

25. V. Loddo, M. Bellardita, G. Camera-Roda, F. Parrino, and L. Palmisano, "Chapter 1-Heterogeneous Photocatalysis: A Promising Advanced Oxidation Process," in *Current Trends and Future Developments on (Bio-) Membranes*, ed. A. Basile, S. Mozia, and R. Molinari (Elsevier, 2018), 1–43, https://doi.org/10.1016/B978-0-12-813549-5.00001-3.

26. A. Hernández-Gordillo, M. Arroyo, R. Zanella, and V. Rodríguez-González, "Photoconversion of 4-Nitrophenol in the Presence of Hydrazine With AgNPs-TiO2 Nanoparticles Prepared by the Sol–Gel Method," *Journal of Hazardous Materials* 268 (2014): 84–91, https://doi.org/10.1016/j.jhazmat.2013.12.069.

27. K. T. Ranjit and B. Viswanathan, "Photoelectrochemical Reduction of Nitrite Ions to Ammonia on CdS Photocatalysts," *Journal of Photochemistry and Photobiology A: Chemistry* 154, no. 2-3 (2003): 299–302, https://doi.org/10.1016/S1010-6030(02)00271-X.

28. J. Chen, S. Qin, G. Song, T. Xiang, F. Xin, and X. Yin, "Shape-Controlled Solvothermal Synthesis of Bi2S3 for Photocatalytic Reduction of CO2 to Methyl Formate in Methanol," *Dalton Transactions* 42 (2013): 15133–15138, https://doi.org/10.1039/C3DT51887F.

29. S. Min and G. Lu, "Dye-Sensitized Reduced Graphene Oxide Photocatalysts for Highly Efficient Visible-Light-Driven Water Reduction," *Journal of Physical Chemistry C* 115, no. 28 (2011): 13938–13945, https://doi.org/10.1021/jp203750z.

30. X. Pan, I. Medina-Ramirez, R. Mernaugh, and J. Liu, "Nanocharacterization and Bactericidal Performance of Silver Modified Titania Photocatalyst," *Colloids and Surfaces B: Biointerfaces* 77, no. 1 (2010): 82–89, https://doi.org/10.1016/j.colsurfb.2010.01.010.

2962, 2026, 1, Downloaded from https://onlinelibrary.wiley.com/doi/10.1155/joch/1225741 by Sonia Mancipe Estevez - Cochrane Colombia , Wiley Online Library on [29/01/2026]. See the Terms and Conditions (https://onlinelibrary.wiley.com/terms-and-conditions) on Wiley Online Library for rules of use; OA articles are governed by the applicable Creative Commons License

31. H.-L. Cao, C. Liu, F.-Y. Cai, et al., "In Situ Immobilization of Ultra-Fine Ag Nps Onto Magnetic Ag@RF@Fe3O4 Core-Satellite Nanocomposites for the Rapid Catalytic Reduction of Nitrophenols," *Water Research* 179 (2020): 115882, https://doi.org/10.1016/j.watres.2020.115882.

32. O. Tokode, R. Prabhu, L. A. Lawton, and P. K. J. Robertson, "Controlled Periodic Illumination in Semiconductor Photocatalysis," *Journal of Photochemistry and Photobiology A: Chemistry* 319-320 (2016): 319–320, https://doi.org/10.1016/j.jphotochem.2015.12.002.

33. M. Rajamathi, G. S. Thomas, and P. V. Kamath, "The Many Ways of Making Anionic Clays," *Journal of Chemical Sciences* 113, no. 5-6 (2001): 671–680, https://doi.org/10.1007/BF02708799.

34. T. B. Nguyen, C. P. Huang, and R. Doong, "Enhanced Catalytic Reduction of Nitrophenols by Sodium Borohydride Over Highly Recyclable Au@Graphitic Carbon Nitride Nanocomposites," *Applied Catalysis B* 240 (2019): 337–347, https://doi.org/10.1016/j.apcatb.2018.08.035.

35. K. Gerelbaatar, A. Tsogoo, R. Dashzeveg, E.-O. Ganbold, and E. O. Ganbold, "Reduction of 2,4-Dinitrophenol to 2,4-Diaminophenol Using AuNPs and AgNPs as Catalyst," *Solid State Phenomena* 271 (2018): 76–84, https://doi.org/10.4028/www.scientific.net/SSP.271.76.

36. A. G. Ramu, M. L. A. Kumari, M. S. Elshikh, H. H. Alkhamis, A. F. Alrefaei, and D. Choi, "A Facile and Green Synthesis of CuO/NiO Nanoparticles and Their Removal Activity of Toxic Nitro Compounds in Aqueous Medium," *Chemosphere* 271 (2021): 129475, https://doi.org/10.1016/j.chemosphere.2020.129475.

37. P. P. Cho, P. P. Mon, D. Vidyasagar, G. Madras, and Ch. Subrahmanyam, "Photocatalytic Reduction of Mono, Di, and Tri-Nitrophenols Over a Bi2MoO6/Carbon Nitride Heterojunction," *New Journal of Chemistry* 47, no. 38 (2023): 17775–17782, https://doi.org/10.1039/D3NJ03243D.

38. G. Yadav, N. Yadav, S. Roy, R. K. Sharma, G. R. Chaudhary, and Md. Ahmaruzzaman, "Sustainable Z-Scheme Photoreduction of Chromium and 2,4,6-Trinitrophenol Using Mn3O4/TiO2-Infused Hydroxyapatite Catalyst Derived From Fish Scales," *Journal of Environmental Chemical Engineering* 13, no. 2 (2025): 116060, https://doi.org/10.1016/j.jece.2025.116060.

39. M. H. Abdellattif and M. Mokhtar, "MgAl-Layered Double Hydroxide Solid Base Catalysts for Henry Reaction: A Green Protocol," *Catalysts* 8, no. 4 (2018): 133, https://doi.org/10.3390/catal8040133.

40. Y. Shen, Y. Wei, J. Ma, et al., "Self-Cleaning Functionalized FeNi/NiFe2O4/NiO/C Nanofibers With Enhanced Microwave Absorption Performance," *Ceramics International* 46, no. 9 (2020): 13397–13406, https://doi.org/10.1016/j.ceramint.2020.02.121.

41. M. M. Rao, B. R. Reddy, M. Jayalakshmi, V. S. Jaya, and B. Sridhar, "Hydrothermal Synthesis of Mg–Al Hydrotalcites by Urea Hydrolysis," *Materials Research Bulletin* 40, no. 2 (2005): 347–359, https://doi.org/10.1016/j.materresbull.2004.10.007.

42. L. Wang, K. Zhang, H. He, W. Sun, Q. Zong, and G. Liu, "Enhanced Corrosion Resistance of MgAl Hydrotalcite Conversion Coating on Aluminum by Chemical Conversion Treatment," *Surface and Coatings Technology* 235 (2013): 484–488, https://doi.org/10.1016/j.surfcoat.2013.08.007.

43. A. Serrano-Lotina, A. J. Martin, M. A. Folgado, and L. Daza, "Dry Reforming of Methane to Syngas Over La-Promoted Hydrotalcite Clay-Derived Catalysts," *International Journal of Hydrogen Energy* 37, no. 17 (2012): 12342–12350, https://doi.org/10.1016/j.ijhydene.2012.06.041.

44. W. W. Focke, D. Molefe, F. J. W. Labuschagne, and S. Ramjee, "The Influence of Stearic Acid Coating on the Properties of Magnesium Hydroxide, Hydromagnesite, and Hydrotalcite Powders," *Journal of Materials Science* 44, no. 22 (2009): 6100–6109, https://doi.org/10.1007/s10853-009-3844-6.

45. B. K. Salem, M. A. Toumi, and O. Internationals, "Comparison of Different Synthesis Ways for Mg–Al- Layered Double Hydroxides (LDH): Effects of Ultrasound Treatment and Characterization of the Structural Phases by Rietveld Refinement," (2017), https://api.semanticscholar.org/CorpusID:13019515.

46. S. Kannan, "Influence of Synthesis Methodology and Post Treatments on Structural and Textural Variations in MgAlCO3 Hydrotalcite," *Journal of Materials Science* 39, no. 21 (2004): 6591–6596, https://doi.org/10.1023/B:JMSC.0000044900.22280.93.

47. K. Warmuz and D. Madej, "Effect of the Particle Size on the Reactivity of MgO-Al2O3 Hydrating Mixtures: A Long-Term Kinetic Investigation of Hydrotalcite Synthesis," *Applied Clay Science* 211 (2021): 106196, https://doi.org/10.1016/j.clay.2021.106196.

48. S. K. Sharma, P. K. Kushwaha, V. K. Srivastava, S. D. Bhatt, and R. V Jasra, "Effect of Hydrothermal Conditions on Structural and Textural Properties of Synthetic Hydrotalcites of Varying Mg/Al Ratio," *Industrial & Engineering Chemistry Research* 46, no. 14 (2007): 4856–4865, https://doi.org/10.1021/ie061438w.

49. J.-W. Kou, S.-Y. Cheng, J.-W. Wang, and X.-M. Xie, "Synthesis and Characterization of Cu/Cr Hydrotalcite-Like Compounds and Their Highly Efficient Application in Catalytic Synthesis of Benzoin Methyl Ether," *Chemical Engineering Journal* 323 (2017): 565–571, https://doi.org/10.1016/j.cej.2017.04.125.

50. L. Cocheci, P. Barvinschi, R. Pode, E. Popovici, and E. Seftel, "Structural Characterization of Some Mg/Zn-Al Type Hydrotalcites Prepared for Chromate Sorption From Wastewater," *Chemical Bulletin* 55 (2010).

51. Y. Shen, D. Liu, L. Fan, S. Li, and L. Gao, "Simultaneous Incorporation of Palladium and Zirconium Ions in Mg–Al Layered Double Hydroxides by Co-Precipitation," *Applied Clay Science* 54, no. 2 (2011): 179–183, https://doi.org/10.1016/j.clay.2011.08.007.

52. J. T. Kloprogge and R. L. Frost, "Fourier Transform Infrared and Raman Spectroscopic Study of the Local Structure of Mg-Ni-and Co-Hydrotalcites," *Journal of Solid State Chemistry* 146, no. 2 (1999): 506–515, https://doi.org/10.1006/jssc.1999.8413.

53. H. Heriyanto, E. Heraldy, and K. Dwi Nugrahaningtyas, "X-RAY Diffraction and Fourier Transform Infrared Study of ca-mg-al Hydrotalcite From Artificial Brine Water With Synthesis Hydrothermal Treatments," *IOP Conference Series: Materials Science and Engineering* 333 (2018): 012006, https://doi.org/10.1088/1757-899X/333/1/012006.

54. J. T. Kloprogge, L. Hickey, and R. L. Frost, "FT-Raman and FT-IR Spectroscopic Study of Synthetic Mg/Zn/Al-Hydrotalcites," *Journal of Raman Spectroscopy* 35, no. 11 (2004): 967–974, https://doi.org/10.1002/jrs.1244.

55. K. S. W. Sing, "Reporting Physisorption Data for Gas/Solid Systems With Special Reference to the Determination of Surface Area and Porosity (Recommendations 1984)," *Pure and Applied Chemistry* 57, no. 4 (1985): 603–619, https://doi.org/10.1351/pac198557040603.

56. E. M. Sabbar, M. E. de Roy, and F. Leroux, "New Cu and/or Pt Complexes Intercalated MgAl-Hydrotalcite-Type Anionic Clays: Synthesis, Characterization, Thermal Behavior and Textural Properties," *Microporous and Mesoporous Materials* 103, no. 1-3 (2007): 134–141, https://doi.org/10.1016/j.micromeso.2007.01.044.

57. C. Chen, J.-C. Buffet, and D. O'Hare, "Surface Modification of Aqueous Miscible Organic Layered Double Hydroxides (AMO-LDHs)," *Dalton Transactions* 49, no. 25 (2020): 8498–8503, https://doi.org/10.1039/D0DT01213K.

58. X. Guo, D. Gao, H. He, et al., "Promotion of CO2 Methanation at Low Temperature Over Hydrotalcite-Derived Catalysts-Effect of the Tunable Metal Species and Basicity," *International Journal of Hydrogen Energy* 46, no. 1 (2021): 518–530, https://doi.org/10.1016/j.ijhydene.2020.09.193.

59. S. Chaudhary, Y. Kaur, B. Jayee, G. R. Chaudhary, and A. Umar, "NiO Nanodisks: Highly Efficient Visible-Light Driven Photocatalyst, Potential

2962, 2026, 1, Downloaded from https://onlinelibrary.wiley.com/doi/10.1155/joch/1225741 by Sonia Mancipe Estevez - Cochrane Colombia , Wiley Online Library on [29/01/2026]. See the Terms and Conditions (https://onlinelibrary.wiley.com/terms-and-conditions) on Wiley Online Library for rules of use; OA articles are governed by the applicable Creative Commons License

Scaffold for Seed Germination of Vigna Radiata and Antibacterial Properties," *Journal of Cleaner Production* 190 (2018): 563–576, https://doi.org/10.1016/j.jclepro.2018.04.110.

60. S. Qiao, C. Feng, Y. Guo, et al., "CdS Nanoparticles Modified Ni@Nio Spheres as Photocatalyst for Oxygen Production in Water Oxidation System and Hydrogen Production in Water Reduction System," *Chemical Engineering Journal* 395 (2020): 125068, https://doi.org/10.1016/j.cej.2020.125068.

61. A. Sharma and B.-K. Lee, "Integrated Ternary Nanocomposite of TiO2/NiO/Reduced Graphene Oxide as a Visible Light Photocatalyst for Efficient Degradation of o-Chlorophenol," *Journal of Environmental Management* 181 (2016): 563–573, https://doi.org/10.1016/j.jenvman.2016.07.016.

62. Y. Piña-Pérez, J. E. Samaniego-Benitez, F. Tzompantzi, et al., "Photocatalytic Hydrogen Production Using Bimetallic and Trimetallic Hydrotalcite as Photocatalysts," *Materials Letters* 330 (2023): 133205, https://doi.org/10.1016/j.matlet.2022.133205.

63. C. Castañeda, I. Alvarado, J. J. Martínez, M. H. Brijaldo, F. B. Passos, and H. Rojas, "Enhanced Photocatalytic Reduction of 4-Nitrophenol Over Ir/CeO2 Photocatalysts Under UV Irradiation," *Journal of Chemical Technology and Biotechnology* 94, no. 8 (2019): 2630–2639, https://doi.org/10.1002/jctb.6072.

64. M. Atarod, M. Nasrollahzadeh, and S. Mohammad Sajadi, "Green Synthesis of Pd/RGO/Fe3O4 Nanocomposite Using Withania Coagulans Leaf Extract and Its Application as Magnetically Separable and Reusable Catalyst for the Reduction of 4-Nitrophenol," *Journal of Colloid and Interface Science* 465 (2016): 249–258, https://doi.org/10.1016/j.jcis.2015.11.060.

65. A. Hernández-Gordillo, A. G. Romero, F. Tzompantzi, S. Oros-Ruiz, and R. Gómez, "Visible Light Photocatalytic Reduction of 4-Nitrophenol Using CdS in the Presence of Na2SO3," *Journal of Photochemistry and Photobiology A: Chemistry* 257 (2013): 44–49, https://doi.org/10.1016/j.jphotochem.2013.02.016.

66. M. Sanyal and U. Sharma, "PAMAM (Poly-Amido Amine) Dendrimer Supported Copper Nanoparticles for Chemoselective Nitro Reduction," *Journal of the Indian Chemical Society* 98, no. 10 (2021): 100149, https://doi.org/10.1016/j.jics.2021.100149.

67. T. Akhtar, A. J. Hill, A. Bhat, et al., "Fabrication of Ruthenium Doped Ag@TiO2 Core-Shell Nanophotocatalyst for the Efficient Reduction of Nitrophenols," *Applied Surface Science* 630 (2023): 157491, https://doi.org/10.1016/j.apsusc.2023.157491.

68. S. Walia, M. Kaur, and S. K. Kansal, "Adsorptive Removal of 2,4-Dinitrophenol From Aqueous Phase Using Amine Functionalized Metal Organic Framework (NH2-MIL-101(Cr))," *Materials Chemistry and Physics* 289 (2022): 126493, https://doi.org/10.1016/j.matchemphys.2022.126493.

69. A. M. Abu-Dief, L. H. Abdel-Rahman, M. A. A. Sayed, M. M. Zikry, M. E. Khalifa, and N. M. El-Metwaly, "Optimization Strategy for Green Synthesis of Silver Nanoparticles (AgNPs) as Catalyst for the Reduction of 2,4-Dinitrophenol Via Supported Mechanism," *Applied Physics A* 128, no. 7 (2022): 595, https://doi.org/10.1007/s00339-022-05704-9.

70. T. Akhtar, A. J. Hill, S. A. Batool Bukhari, H. Nasir, S. Ullah, and J. W. Schwank, "Fabrication of 2D/0D ZnO/CuO Z-Scheme Heterojunctions for Enhanced Photocatalytic Reduction of 2,4-Dinitrophenol and 2,4,6-Trinitrophenol Under Visible Light," *Solar Energy* 289 (2025): 113330, https://doi.org/10.1016/j.solener.2025.113330.

71. S. Ranjan Mishra, V. Gadore, J. Sahu, K. Parida, and Md. Ahmaruzzaman, "Green Synthesis of In2S3-Supported Ni-MOF: Bifunctional Photocatalyst for Sustainable H2O2 Production and 2,4,6-Trinitrophenol Photoreduction," *Solar Energy* 282 (2024): 112943, https://doi.org/10.1016/j.solener.2024.112943.

72. Y. R. Mejía and N. K. Reddy Bogireddy, "Reduction of 4-Nitrophenol Using Green-Fabricated Metal Nanoparticles," *RSC Advances* 12, no. 29 (2022): 18661–18675, https://doi.org/10.1039/D2RA02663E.

73. P. Pati, S. McGinnis, and P. Vikesland, "Life Cycle Assessment of "Green" Nanoparticle Synthesis Methods," *Environmental Engineering Science* 31, no. 7 (2014): 410–420, https://doi.org/10.1089/ees.2013.0444.

74. S. Gu, S. Wunder, Y. Lu, et al., "Kinetic Analysis of the Catalytic Reduction of 4 Nitrophenol by Metallic Nanoparticles," *Journal of Physical Chemistry C* 118, no. 32 (2014): 18618–18625, https://doi.org/10.1021/jp5060606.

2962, 2026, 1, Downloaded from https://onlinelibrary.wiley.com/doi/10.1155/joch/1225741 by Sonia Mancipe Esevez - Cochrane Colombia , Wiley Online Library on [29/01/2026]. See the Terms and Conditions (https://onlinelibrary.wiley.com/terms-and-conditions) on Wiley Online Library for rules of use; OA articles are governed by the applicable Creative Commons License